Microwave Diversity Imaging of Perfectly Conducting Objects in the Near-Field Region

Tah-Hsiung Chu, *Member, IEEE*, and Ding-Bing Lin

***Abstract*—In this paper, analytical and numerical studies of microwave diversity imaging of continuous and discrete conducting objects in the near-field region are presented. Analytical results show that the image of the scattering object can be reconstructed via Fourier inversion of the data acquired from the recorded scattered field using angular and frequency diversity techniques. Furthermore, different feature information of the scattering object can be obtained using a polarization diversity technique. Various scattering arrangements are studied and compared on the basis of the reconstructed image quality and practical considerations. Numerical results show that the described frequency, angular, and polarization diversity techniques in the backward scattering arrangement can be a cost-effective approach in near-field microwave imaging systems.**

I. Introduction

MICROWAVE imaging is cataloged as an inverse scattering problem [1], one in which the physical properties, such as geometrical shape or material characteristics, of the unknown scattering object are deduced from the measured scattered field data. Approaches to reconstruct microwave images of the scattering objects are usually based on the theory of direct scattering with certain approximations.

For the case of a perfectly conducting object, the physical optics approximation is usually adopted to relate the geometrical shape of the conducting object to its scattered field. It is known that, under the physical optics approximation, Bojarski's identity forms the basis of monostatic microwave imaging of a perfectly conducting object in the far-field region [2], [3]. However, when the test object is located in the near-field region of the receiving aperture, the paraxial approximations of far-field and monostatic imaging geometry cannot be made.

In general, good resolution is the main design objective of an imaging system. The size of the available recording aperture conventionally restricts the resolution capability. The approach followed to improve image resolution of a microwave imaging system involves extending the effective area of the physical recording aperture by means of various synthetic aperture techniques. The use of frequency and angular diversity techniques has been applied and has been found experimentally to yield high-resolution microwave images of conducting objects [4], [5].

Manuscript received August 25, 1989; revised October 21, 1990. This work was supported by the National Science Council, Republic of China, under Grant NSC 79-0404-E002-53.

The authors are with the Electrical Engineering Department, National Taiwan University, Taipei, Taiwan, Republic of China.

IEEE Log Number 9041949.

In this paper, studies of microwave imaging of perfectly conducting objects in the near-field region employing frequency, angular, and polarization diversities are presented. Analytical results show that the image can be reconstructed via Fourier inversion of the acquired Fourier space data based on a theorem that will be developed in Section II. This theorem says that by illuminating conducting objects with a plane wave, two-dimensional Fourier transformation of the measured scattered field on a planar receiving array will give values of the three-dimensional Fourier transformation of the scattering function distributed on a spherical surface in the Fourier space.

According to the formulation of image reconstruction to be developed in Section II, the Fourier space data can be acquired by combining angular and frequency diversities, and information on the various features of the scattering object can be obtained by using the polarization diversity technique. In general, the angular diversity technique is time consuming, since it involves recording the scattered field from all directions. Results of this paper will demonstrate that only a limited number of views are required to reconstruct the image by using the frequency diversity technique. With theoretical and numerical results, the frequency diversity technique is shown to be the most suitable candidate for imaging perfectly conducting objects in the near-field region.

This paper consists of four sections. In Section II, formulations of scattered field and image reconstruction of continuous and discrete scattering objects, are presented, along with a discussion of the use of microwave diversity techniques to acquire the Fourier space data. Numerical results corresponding to various scattering arrangements are given in Section III. Lastly, in Section IV, the findings of this paper are summarized.

II. Theoretical Development

In this section, we will relate the scattering properties to the microwave image reconstruction algorithm for continuous and discrete conducting objects under the illumination of a plane wave in the forward- and backward-scattering near-field arrangements shown in Fig. 1(a) and (b) respectively.

A. Continuous Scattering Object

Considering a perfectly conducting object illuminated by a plane wave with $\exp(j\omega t)$ time dependence, the scattered field $\boldsymbol{E}^s(\boldsymbol{r})$ over a planar array located at $z = d$ (forward-

0018-9480/91/0300-0480$01.00 ©1991 IEEE

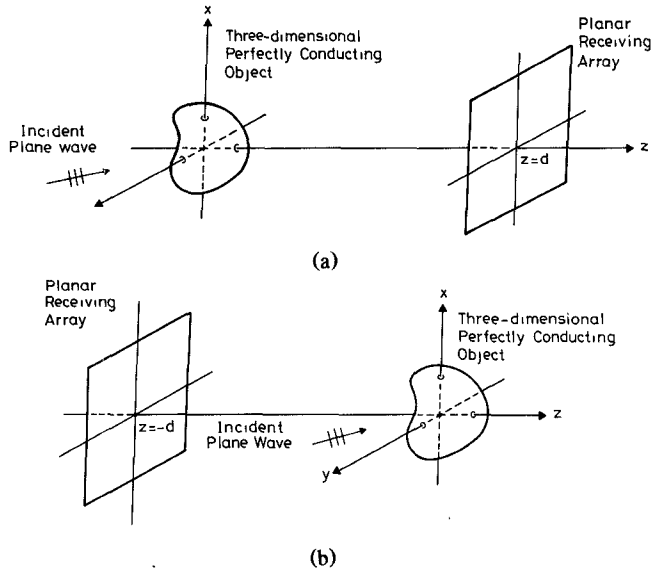

Fig. 1. (a) Forward and (b) backward scattering geometries.

scattering arrangement) or $z = -d$ (backward-scattering arrangement) in the near-field region of the scattering object is given as

$$\boldsymbol{E}^s(x, y, z = \pm d) = -j\omega\mu_0 \iint \bar{\bar{G}}(|\boldsymbol{r} - \boldsymbol{r}'|) \cdot \boldsymbol{J}_s(\boldsymbol{r}')\, d^2\boldsymbol{r}' \quad (1)$$

where

$$\bar{\bar{G}}(|\boldsymbol{r} - \boldsymbol{r}'|) = \left\{ \bar{\bar{I}} + \frac{\nabla\nabla}{k_0^2} \right\} G(|\boldsymbol{r} - \boldsymbol{r}'|) \quad (2)$$

is the dyadic Green's function in free space, $\bar{\bar{I}}$ is the unit dyadic, $G(|\boldsymbol{r} - \boldsymbol{r}'|)$ is the Green's function in free space, $\boldsymbol{J}_s(\boldsymbol{r}')$ is the induced surface current density, $k_0 = \omega/c$, and $d^2\boldsymbol{r}'$ is a surface element.

When the dimension of the object is much larger than the wavelength of illumination, or the physical optics approximation [6], the kernel of the integral in (1) becomes

$$\bar{\bar{G}}(|\boldsymbol{r} - \boldsymbol{r}'|) \cdot \boldsymbol{J}_s(\boldsymbol{r}') = \bar{\bar{I}} G(|\boldsymbol{r} - \boldsymbol{r}'|) \cdot [2\hat{n}(\boldsymbol{r}') \times \boldsymbol{H}^i(\boldsymbol{r}')] + \frac{\nabla\nabla}{k_0^2} G(|\boldsymbol{r} - \boldsymbol{r}'|) \cdot [2\hat{n}(\boldsymbol{r}') \times \boldsymbol{H}^i(\boldsymbol{r}')] \quad (3)$$

where

$$\boldsymbol{H}^i(\boldsymbol{r}') = H_0 e^{-j\boldsymbol{k}_0 \cdot \boldsymbol{r}'} \hat{a}_h \quad (4)$$

is the incident plane wave with wave vector $\boldsymbol{k}_0 = k_0 \hat{a}_k$, and the unit vector $\hat{a}_h$ is perpendicular to $\boldsymbol{k}_0$.

Assume that the geometry of the illuminated conducting object and the polarization state of the incident wave are appropriate, as, for example, in the case considered in the numerical simulation studies in Section III with a TM polarization wave incident on a cylindrical object. The first term in the right side of (3) is much more dominant than the second term, i.e.,

$$\bar{\bar{I}} G(|\boldsymbol{r} - \boldsymbol{r}'|) \cdot [2\hat{n}(\boldsymbol{r}') \times \boldsymbol{H}^i(\boldsymbol{r}')] \gg \frac{\nabla\nabla}{k_0^2} G(|\boldsymbol{r} - \boldsymbol{r}'|) \cdot [2\hat{n}(\boldsymbol{r}') \times \boldsymbol{H}^i(\boldsymbol{r}')]. \quad (5)$$

Thus the dyadic Green's function $\bar{\bar{G}}(|\boldsymbol{r} - \boldsymbol{r}'|)$ in (2) can then be reduced to the scalar Green's function $G(|\boldsymbol{r} - \boldsymbol{r}'|)$ and (1) becomes

$$\boldsymbol{E}^s(x, y, z = \pm d, \boldsymbol{k}_0) = -j\omega\mu_0 H_0 \iint_{S_{\text{ill}}} 2\hat{n}(\boldsymbol{r}') \times \hat{a}_h e^{-j\boldsymbol{k}_0 \cdot \boldsymbol{r}'} G(|\boldsymbol{r} - \boldsymbol{r}'|)\, d^2\boldsymbol{r}' \quad (6)$$

where the surface integral is over the object illuminated region S_{ill}.

Given that the polarization state of each receiving element is in the same direction $\hat{p}$, the recorded scattered field becomes a scalar form as

$$U^s(x, y, z = \pm d, \boldsymbol{k}_0) = \hat{p} \cdot \boldsymbol{E}^s(x, y, z = \pm d, \boldsymbol{k}_0) = -j\omega\mu_0 H_0 \iiint O(\boldsymbol{r}') e^{-j\boldsymbol{k}_0 \cdot \boldsymbol{r}'} G(|\boldsymbol{r} - \boldsymbol{r}'|)\, d^3\boldsymbol{r}' \quad (7)$$

where

$$O(\boldsymbol{r}') = \hat{p} \cdot (2\hat{n}(\boldsymbol{r}') \times \hat{a}_h) \delta(S(\boldsymbol{r}')) \quad (8)$$

is defined as the scattering function, which is related to the polarization states of the transmitting and receiving antennas and the illuminated surface of the conducting object, and $\delta(\cdot)$ is a one-dimensional Dirac delta function with its argument defined as

$$S(\boldsymbol{r}') \begin{cases} = 0 & \text{as } \boldsymbol{r}' \in S_{\text{ill}} \\ \neq 0 & \text{elsewhere} \end{cases} \quad (9)$$

to reduce the volume integral in (7) to the surface integral in (6).

By expressing the wave vector $\boldsymbol{k}_0$ of the incident plane wave as $\boldsymbol{k}_0 = k_{x0}\hat{x} + k_{y0}\hat{y} + k_{z0}\hat{z}$ and using the plane wave expansion of the Green's function [7]

$$G(|\boldsymbol{r} - \boldsymbol{r}'|) = \frac{1}{4\pi^2} \cdot \iint \frac{-j}{2k_z} e^{-jk_z|\pm d - z'|} e^{-j[k_x(x-x') + k_y(y-y')]}\, dk_x\, dk_y \quad (10)$$

where

$$k_z = \begin{cases} \sqrt{k_0^2 - k_x^2 - k_y^2} & \text{as } \sqrt{k_x^2 + k_y^2} \leq k_0 \\ -j\sqrt{k_x^2 + k_y^2 - k_0^2} & \text{as } \sqrt{k_x^2 + k_y^2} > k_0 \end{cases} \quad (11)$$

(7) becomes

$$U^s(x, y, z = \pm d, \boldsymbol{k}_0) = \frac{1}{4\pi^2} \iint \frac{-\omega\mu_0 H_0}{2k_z} e^{-jk_z d} \cdot \left(\iiint O(\boldsymbol{r}') e^{j[(k_x - k_{x0})x' + (k_y - k_{y0})y' + (\pm k_z - k_{z0})z']} d^3\boldsymbol{r}' \right) \cdot e^{-j(k_x x + k_y y)}\, dk_x\, dk_y. \quad (12)$$

A two-dimensional Fourier transform of the resulting expression of $U^s(x, y, z = \pm d, \boldsymbol{k}_0)$ in the x and y directions will yield

$$\tilde{U}^s(k_x, k_y, z = \pm d, \boldsymbol{k}_0) = \frac{-\omega\mu_0 H_0}{2k_z} e^{-jk_z d} \cdot \tilde{O}(k_x - k_{x0}, k_y - k_{y0}, \pm k_z - k_{z0}) \quad (13a)$$

or

$$\tilde{O}(k_x, k_y, k_z) = \frac{\pm 2(k_z + k_{z0})}{-\omega\mu_0 H_0} e^{\pm j(k_z + k_{z0})d} \cdot \tilde{U}^s(k_x + k_{x0}, k_y + k_{y0}, z = \pm d, \boldsymbol{k}_0). \quad (13b)$$

In deriving (13), the two-dimensional Fourier transformation of $U^s(x, y, z = \pm d)$ in the x and y directions is defined as

$$\tilde{U}^s(k_x, k_y, z = \pm d) = \iint U^s(x, y, z = \pm d) e^{j(k_x x + k_y y)} dx\, dy \quad (14)$$

whereas the three-dimensional Fourier transformation of the scattering function $O(\boldsymbol{r})$ of the scattering conducting object is defined as

$$\tilde{O}(\boldsymbol{k}) = \iiint O(\boldsymbol{r}) e^{j\boldsymbol{k}\cdot\boldsymbol{r}} d^3\boldsymbol{r} \quad (15)$$

where $\boldsymbol{k} = k_x\hat{x} + k_y\hat{y} + k_z\hat{z}$ is the wave vector in Fourier space.

After applying (11), the arguments of $\tilde{O}(\boldsymbol{k})$ in (13b) are related by

$$(k_x + k_{x0})^2 + (k_y + k_{y0})^2 + (k_z + k_{z0})^2 = k_0^2. \quad (16)$$

Expression (16) defines a spherical surface in the Fourier space $\tilde{O}(\boldsymbol{k}_0)$ with radius k_0 and its center given by the wave vector $\boldsymbol{k}_0$ of the incident plane wave. Therefore, (13b) shows that proper normalization of the two-dimensional Fourier transformation results of the scattered field recorded by a planar array located at $z = d$ (forward-scattering arrangement) or $z = -d$ (backward-scattering arrangement) yields a semispherical surface centered at $(-k_{x0}, -k_{y0}, -k_{z0})$ with radius k_0 in the three-dimensional Fourier space $\tilde{O}(\boldsymbol{k})$. Note that (13) is similar to the formulation of the diffraction tomography of a dielectric object satisfying the Born approximation [7] except for the definition of the scattering function and the normalization factor relating $\tilde{U}^s$ and $\tilde{O}(\boldsymbol{k})$.

The microwave image of the continuous scattering object, defined by the scattering function $O(r)$ given in (8), can then be reconstructed through Fourier inversion of the recorded scattered field $U^s(x, y, z = \pm d, \boldsymbol{k}_0)$ by varying the incident wave vector $\boldsymbol{k}_0$, the observation angle of the receiving aperture (frequency and angular diversity), and the polarization states $\hat{p}$ and/or $\hat{a}_h$ (polarization diversity) to acquire the Fourier space data $\tilde{O}(\boldsymbol{k})$. Details of the microwave diversity techniques to acquire the Fourier space data will be discussed in subsection C.

B. Discrete Scattering Object

Assume the discrete scatterers are isotropic scattering points and there is no mutual coupling between the scatterers. The scalar scattered field $E^s(\boldsymbol{r})$ over a planar array located at $z = d$ (forward-scattering arrangement) or $z = -d$ (backward-scattering arrangement) in the near-field region of the scattering object can be expressed as

$$E^s(x, y, z = \pm d, \boldsymbol{k}_0) = \sum_i \sigma(\boldsymbol{r}_i') E^i(\boldsymbol{r}_i') G(|\boldsymbol{r} - \boldsymbol{r}_i'|) \quad (17)$$

where

$$E^i(\boldsymbol{r}_i') = E_0 e^{-j\boldsymbol{k}_0\cdot\boldsymbol{r}_i'} \quad (18)$$

is the incident plane wave and $\sigma(\boldsymbol{r}_i')$ is the reflectivity of the point scatterer at $\boldsymbol{r}_i'$.

By defining the scattering function as

$$O(\boldsymbol{r}) = \sum_i \sigma(\boldsymbol{r}_i') \delta(\boldsymbol{r} - \boldsymbol{r}_i') \quad (19)$$

where $\delta(\boldsymbol{r} - \boldsymbol{r}_i')$ is a three-dimensional Dirac delta function, the summation in (17) becomes the volume integral given as

$$U^s(x, y, z = \pm d, \boldsymbol{k}_0) = E^s(x, y, z = \pm d, \boldsymbol{k}_0) = E_0 \iiint O(\boldsymbol{r}') e^{-j\boldsymbol{k}_0\cdot\boldsymbol{r}'} G(|\boldsymbol{r} - \boldsymbol{r}'|)\, d^3\boldsymbol{r}'. \quad (20)$$

Note that (20) is similar to (7) except for the scaling factor outside the integral. Therefore, by substituting (10) into (20) and performing two-dimensional Fourier transformation of the resulting expression of $U^s(x, y, z = \pm d, \boldsymbol{k}_0)$ in the x and y directions, an expression similar to (13) can be obtained:

$$\tilde{U}^s(k_x, k_y, z = \pm d, \boldsymbol{k}_0) = \frac{-jE_0}{2k_z} e^{-jk_z d} \cdot \tilde{O}(k_x - k_{x0}, k_y - k_{y0}, \pm k_z - k_{z0}) \quad (21a)$$

or

$$\tilde{O}(k_x, k_y, k_z) = \frac{\pm 2(k_z + k_{z0})}{-jE_0} e^{\pm j(k_z + k_{z0})d} \cdot \tilde{U}^s(k_x + k_{x0}, k_y + k_{y0}, z = \pm d, \boldsymbol{k}_0). \quad (21b)$$

Therefore, microwave images of discrete scattering objects, defined by the scattering function $O(\boldsymbol{r})$ given in (19), which in turn is related to the reflectivity and the distribution of each point scatterer, can be reconstructed from the recorded scattered field $U^s(x, y, z = \pm d, \boldsymbol{k}_0)$ by varying the incident wave vector $\boldsymbol{k}_0$ and the observation angle of the receiving aperture (frequency and angular diversity) to acquire the Fourier space data $\tilde{O}(\boldsymbol{k})$.

In the next subsection, studies of image reconstruction for continuous and discrete scattering objects using microwave diversity techniques to acquire the Fourier space data based on the formulation derived above will be given for the two-dimensional case for simplicity.

C. Microwave Diversity Techniques

In a two-dimensional arrangement the scattering object is assumed to be infinitely long in the y direction and the receiving aperture is a linear array in the x direction located at $z = d$ or $z = -d$ (i.e., forward or backward scattering arrangement). For a plane wave illumination with fixed wave vector $\boldsymbol{k}_0 = k_0\hat{z}$, only circular shaped Fourier components $\tilde{O}(k_x, k_z)$, as illustrated in Fig. 2(a) and (b), are accessible from the recorded scattered field. Note that when the linear array is placed in the forward-scattering arrangement (i.e., $z = d$), the locus represented by (16) and k_z ranging from $-k_0$ to 0 becomes a semicircle denoted by the solid line

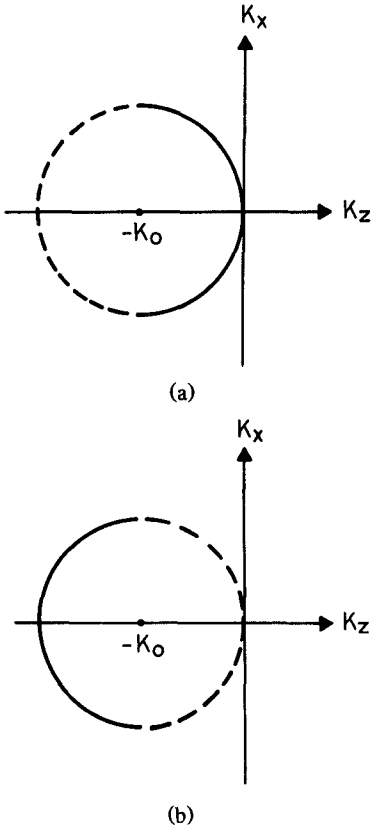

Fig. 2. Fourier slices acquired in (a) forward and (b) backward scattering arrangements with single-frequency (wavenumber k_0) plane wave illumination.

shown in Fig. 2(a). In Fig. 2(b), the semicircle denoted by the solid line, with k_z ranging from $-2k_0$ to $-k_0$, is obtained by placing the linear array in the backward-scattering arrangement (i.e., $z = -d$).

In order to reconstruct the image of the scattering function with high resolution, a large portion of Fourier space data is required, i.e., additional degrees of freedom to acquire the Fourier space data are necessary. Note that in the above derivation there are three variables that can be exploited to acquire the Fourier space data: i.e., $\boldsymbol{k}_0$, $\hat{p}$, and $\hat{a}_h$. In the following, we will discuss three microwave diversity measurement techniques using these three degrees of freedom.

1) *Angular Diversity Technique:* By rotating the scattering object over a full 360° in small steps, the circular shaped Fourier components $\tilde{O}(k_x, k_z)$ will rotate in like manner. These semicircles will then trace a disk of radius $\sqrt{2}k_0$ centered at the origin for the case of the forward-scattering arrangement as shown in Fig. 3(a), or an annular ring of inner radius $\sqrt{2}k_0$ and outer radius $2k_0$ for the case of the backward-scattering arrangement, as shown in Fig. 3(b). However, because of the double coverage of the Fourier domain generated by the semicircles illustrated in Fig. 3(a) and (b), the Fouier components $\tilde{O}(k_x, k_z)$ corresponding to either the positive or the negative k_x should be discarded to eliminate redundancy.
2) *Frequency Diversity Technique:* By linearly stepping the frequency of the incident wave from f_1 to f_2 (wavenumber varying from k_1 to k_2), the radius of two semicircular slices denoted by the solid lines in Fig. 2(a) and (b) extend to a crescent-shaped section and a fan-shaped section in the Fourier space respectively, as shown in Fig. 4(a) and (b). Therefore, in the backward-scattering arrangement, a total of four views are sufficient to cover most of the Fourier space, while more views are seen to be needed for the forward-scattering case, as illustrated in Fig. 5(a) and (b).
3) *Polarization Diversity:* By changing the polarization states of the transmitting and receiving antennas, different Fourier space data are accessible, and the reconstructed image for each polarization state pair gives information on the different features of the scattering object.

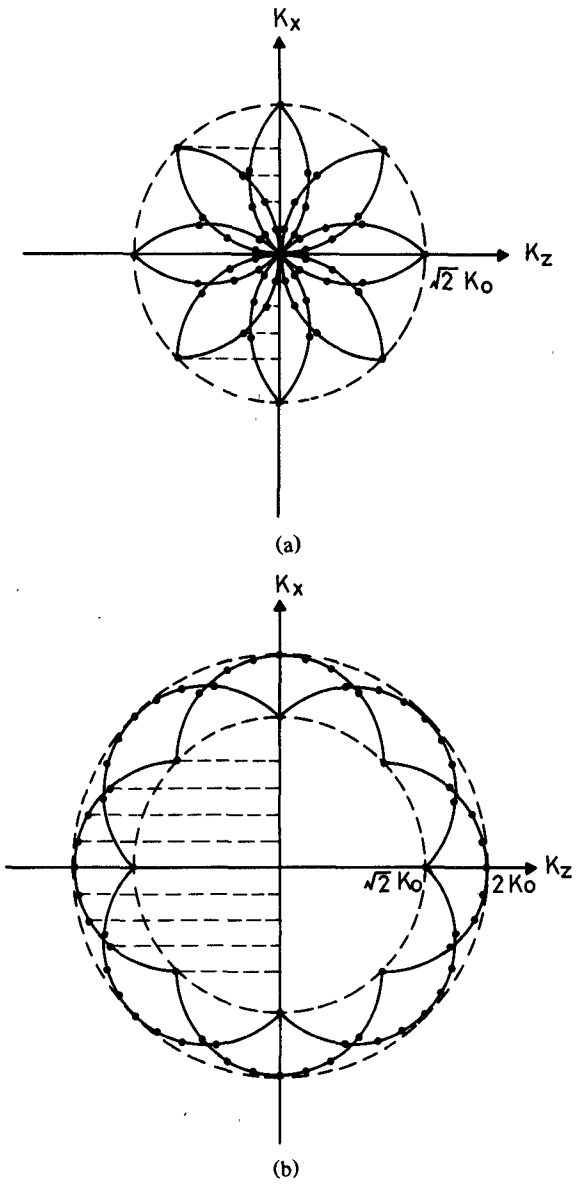

Fig. 3. Fourier space data acquired in (a) forward and (b) backward scattering arrangements using angular diversity technique for 360° viewing angles.

It is quite obvious that the forward-scattering arrangement is a more suitable imaging geometry for the single-frequency

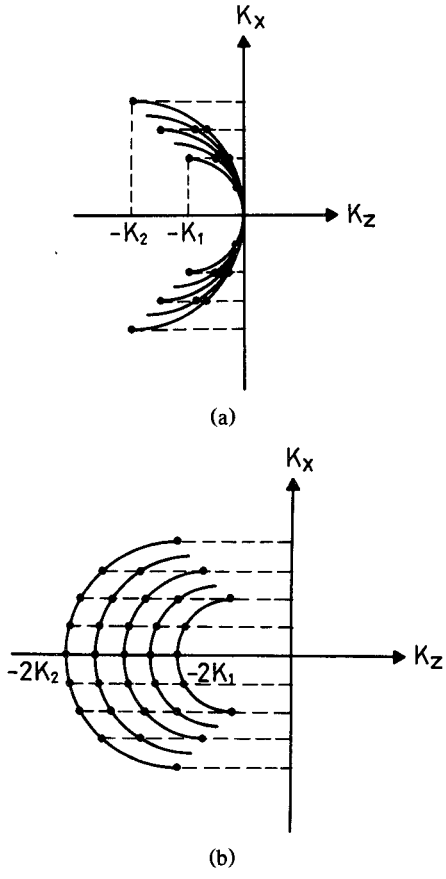

Fig. 4. Fourier space data acquired in (a) forward and (b) backward scattering arrangements using frequency diversity technique with k_0 stepped from k_1 to k_2.

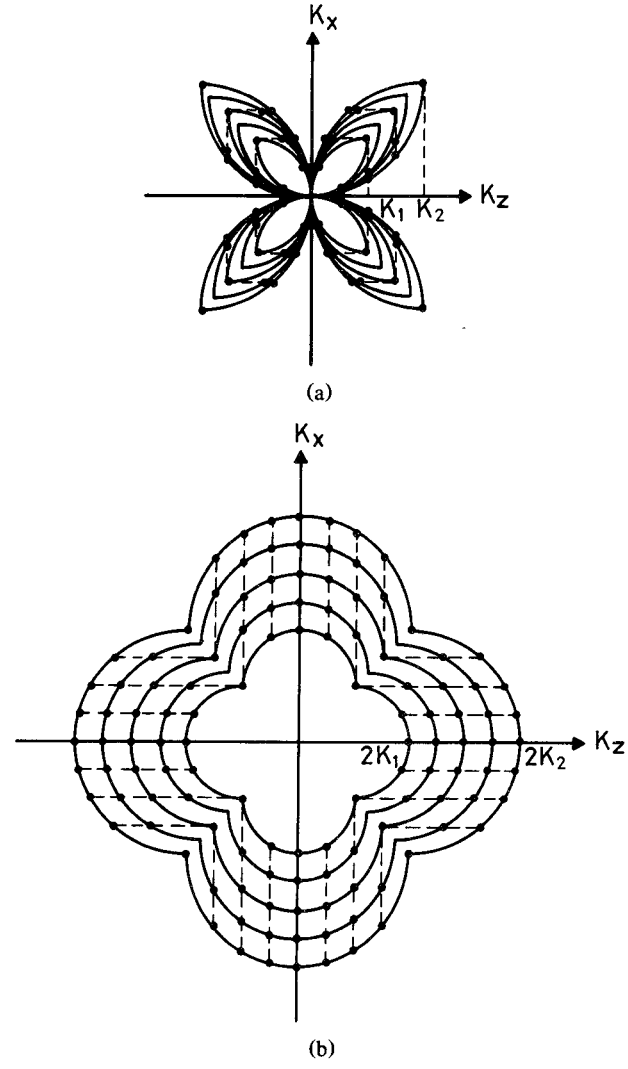

Fig. 5. Fourier space data acquired in (a) forward and (b) backward scattering arrangements using frequency and angular diversity techniques (k_0 stepped from k_1 to k_2, and four orthogonal views).

illumination case, since it can fill a larger portion of the Fourier space than that in the backward-scattering arrangement. However, the angular diversity technique is time consuming in practice and a band-pass version of Fourier space data would yield a similar image of the scattering function given by either (8), describing the shape of a continuous scattering object, or (19), representing the distribution of a discrete scattering object. Therefore, comparing Fig. 3(a) with Fig. 5(b), it is interesting to note that the backward-scattering arrangement using frequency diversity with four views is practically superior to the forward-scattering arrangement using only the angular diversity technique with small steps over 360° viewing angles, provided the frequency range is wide enough. This implies that the described frequency, angular, and polarization diversity techniques in the backward-scattering arrangement can be a cost-effective approach in near-field microwave imaging systems.

In the next section, numerical results of the described two-dimensional near-field microwave imaging system will be presented to illustrate the theoretical development given above.

III. Numerical Results

Numerical examples of continuous and discrete scattering objects are given in this section for two cases, (a) multiview single-frequency forward/backward scattering arrangements and (b) a single-view/four-view multifrequency backward-scattering arrangement, to simulate the theoretical development discussed in Section II. Simulation results of a multifrequency forward-scattering arrangement are not presented, because the synthesized Fourier space practically covers a very small region.

A. Continuous Scattering Object

A perfectly conducting cylinder with radius $a = 15$ cm assumed to be infinitely long in the y direction is used as the test object. A 384-cm-long linear receiving array is located at $z = 30$ cm (forward-scattering arrangement) and $z = -30$ cm (backward-scattering arrangement).

Assume the electric field of the incident plane wave is polarized in the y direction (i.e., TM polarization) and the polarization state of each receiving antenna is in the y direction. Therefore the second term in (3) becomes zero to satisfy the assumption given in (5).

In the simulation study of case (a) (i.e., multiview, single-frequency forward/backward scattering arrangements), the illuminating frequency is 10 GHz, and the scattered field is recorded by a linear receiving array with 256 equally spaced

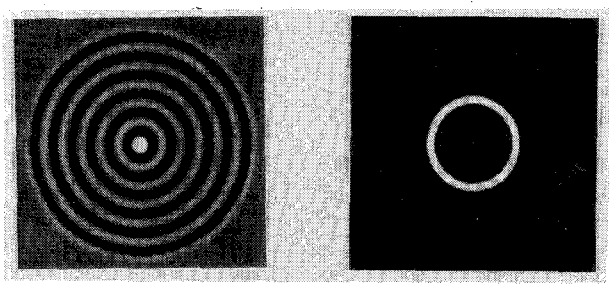

(a) (b)

Fig. 6. (a) Fourier space data of the test conducting cylinder object acquired in the forward scattering arrangement using angular diversity technique and (b) its reconstructed image.

(a) (b)

Fig. 7. (a) Fourier space data of the test conducting cylinder object acquired in the backward scattering arrangement using angular diversity technique and (b) its reconstructed image.

points and a total of 128 equally spaced views over 360°. The simulated two-dimensional Fourier space data $\tilde{O}(k_x, k_z)$ are then reformed in a 128×128 rectangular format, as shown in Fig. 6(a), through the four-nearest-neighbors interpolation algorithm [8] in order to perform two-dimensional inverse FFT.

The reconstructed image from the multiview, single-frequency forward-scattering arrangement is shown in Fig. 6(b). The circular ring image shown in Fig. 6(b) represents the shape of the cylinder and is in good agreement with the object geometry. Since the Fourier space data obtained in the backward-scattering arrangement in Fig. 7(a) cover a very thin annular pattern, the reconstructed image shown in Fig. 7(b) bears a much poorer resemblance to the test object than the result in Fig. 6(b).

In case (b), involving the single-view/four-view multifrequency backward-scattering arrangement, the scattered field along the linear receiving array is sampled at 256 equally spaced points with frequency stepped from 5 to 10 GHz in 32 steps. The range of ka is 15.7–31.4 radians; i.e., the simulation is in the physical optics regime. The simulation results of Fourier space data shown in Fig. 8(a) and (b) correspond to the single view and four orthogonal views respectively. The reconstructed image from the single-view case, as shown in Fig. 9(a), gives a partial circular ring image. This is because the object dimension is much larger than the wavelength used; according to the physical optics approximation the induced surface current is primarily on the surface of the

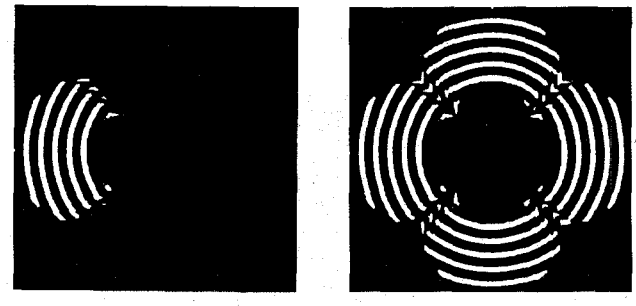

(a) (b)

Fig. 8. Fourier space data of the test conducting cylinder object acquired in the backward scattering arrangement using (a) single view and (b) four orthogonal views with the frequency diversity technique (frequency stepped from 5 GHz to 10 GHz in 32 steps).

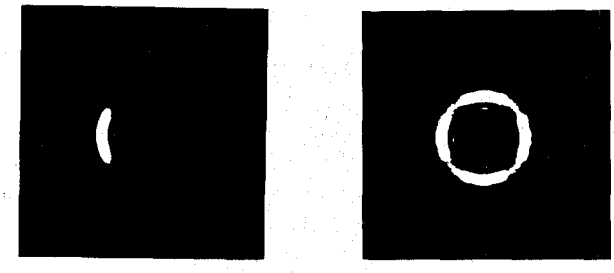

(a) (b)

Fig. 9. Reconstructed image of the test conducting cylinder object obtained from the Fourier space data given in (a) Fig. 8(a) for single view and in (b) Fig. 8(b) for four orthogonal views.

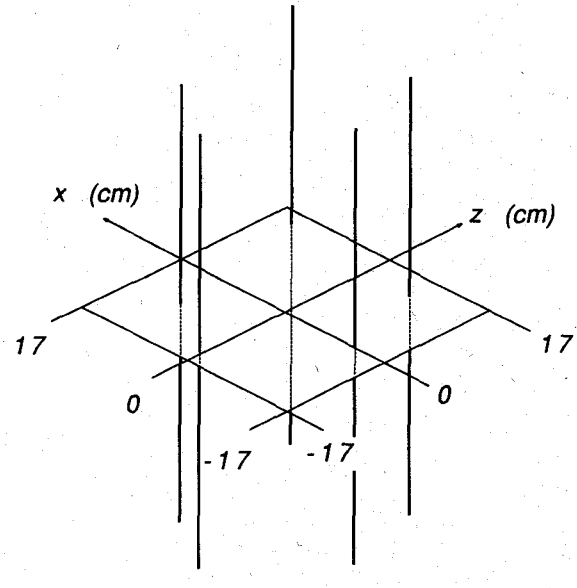

Fig. 10. Simulated line scatterers at $(-15, 0)$ cm, $(-8, 10)$ cm, $(0, -12)$ cm, $(13, -8)$ cm, and $(15, 14)$ cm respectively.

object illuminated region. Therefore, a four-orthogonal-view arrangement is required to reconstruct an image representing the shape of the scattering object, as shown in Fig. 9(b). The image quality is seen to be not as good as that given in Fig. 6(b) because the low-frequency portion is lacking and the Fourier space coverage is smaller than that in Fig. 6(a).

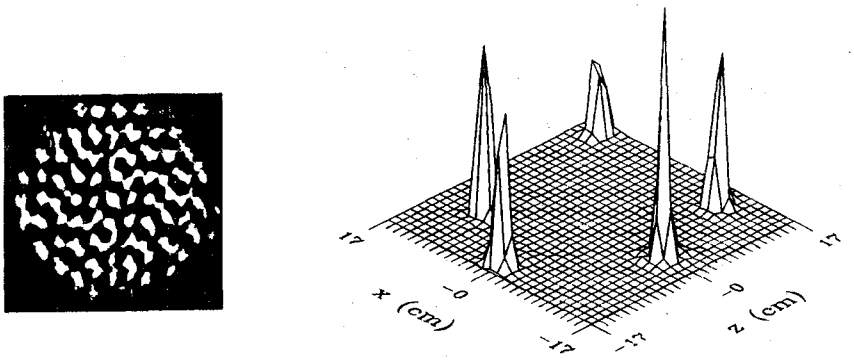

(a) (b)

Fig. 11. (a) Fourier space data of the test discrete object acquired in the forward scattering arrangement using angular diversity technique and (b) its reconstructed image.

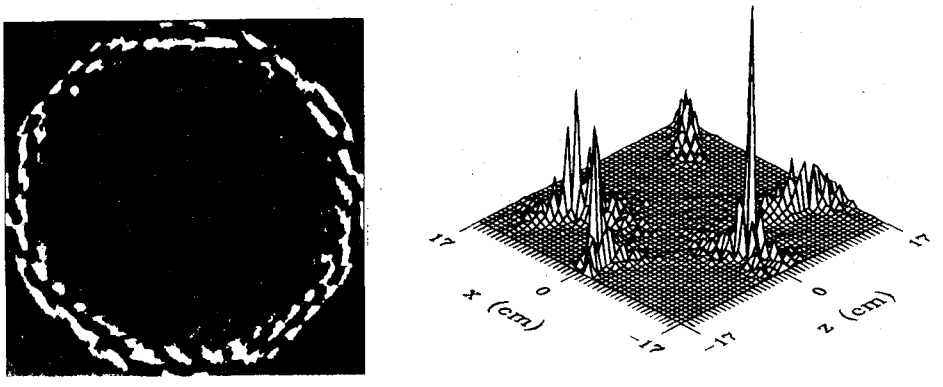

(a) (b)

Fig. 12. (a) Fourier space data of the test discrete object acquired in the backward scattering arrangement using angular diversity technique and (b) its reconstructed image.

However, the multifrequency backward-scattering arrangement provides a cost-effective scheme to record the scattered field compared with the multiview, single-frequency forward-scattering arrangement.

B. Discrete Scattering Object

A two-dimensional discrete conducting object consisting of five line scatterers with equal reflectivity, shown in Fig. 10, is used as the test discrete scattering object for the same two cases given in the first numerical example except that the linear receiving array is 96 cm long in this numerical study.

In the simulation study of case (a) (i.e., the multiview, single-frequency forward/backward scattering arrangements), the illuminating frequency is 10 GHz, and the scattered field is recorded by a linear receiving array with 64 equally spaced points and a total of 128 equally spaced views over 360°. Results of the Fourier space data and reconstructed images of the test discrete object are shown in Figs. 11 and 12 for the cases of forward- and backward-scattering arrangements respectively. The reconstructed image shown in Fig. 12(b) carries much poorer resolution about the test object than the result given in Fig. 11(b), because the Fourier space data obtained in the backward-scattering arrangement shown in Fig. 12(a) cover a very thin annular region. All the reconstructed images shown in Figs. 11(b) and 12(b) are in good agreement with the object geometry except for the different resolutions about the test object.

In case (b), involving the single-view, multifrequency backward-scattering arrangement, the scattered field is recorded by a linear receiving array at 64 equally spaced points with frequency stepped from 5 to 10 GHz in 32 steps. Fig. 13 shows the results of the Fourier space data of the test object and the reconstructed image. The reconstructed image is seen to be in good agreement with the object geometry. Note that in the study of this case the scattered field is recorded using frequency diversity only. A four-view arrangement is not necessary because no shadow region exists for the discrete scattering object.

IV. Conclusions

In this study, the microwave diversity imaging of perfectly conducting objects in the near-field region has been shown to be able to retrieve the shape of continuous scattering objects and the distribution of discrete scattering objects. It has been shown that the backward-scattering arrangement using the frequency diversity technique to acquire the Fourier space data is the most efficient and flexible approach for imaging a conducting object in the near-field region. In the case of a continuous scattering object, the reconstructed image from the backward-scattering arrangement with a sin-

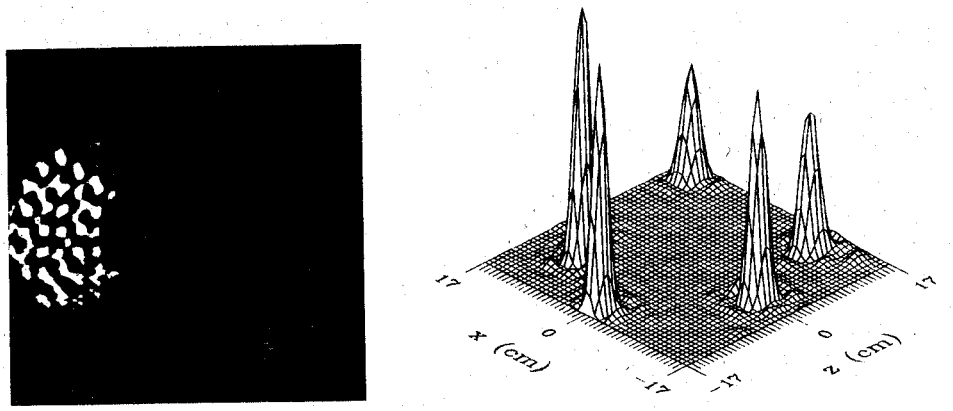

(a) (b)

Fig. 13. (a) Fourier space data of the test discrete object acquired in the backward scattering arrangement using the frequency diversity technique (frequency stepped from 5 GHz to 10 GHz in 32 steps) with single view and (b) its reconstructed image.

gle view yields shape information corresponding to the illuminated surface of the scattering object. Therefore, a total of four orthogonal views using frequency diversity in the backward arrangement are required to reconstruct an image representing the complete shape of the scattering object. In Section III results of various numerical examples illustrate the findings of the developed near-field microwave imaging theorem of perfectly conducting objects.

In this paper, the microwave imaging principle has been analyzed under the assumptions of (5) and the physical optics approximation. It is known that the physical optics approximation is inadequate for scattering problems when the dominant scattering mechanism derives from edge diffraction, multiple reflection, creeping waves or traveling waves. These scattering mechanisms are, however, important contributions to the scattered field of a conducting object of complex shape [9]. Therefore an exact imaging theorem will be needed for a more general near-field microwave imaging system for conducting objects of complex shape.

References

[1] H. P. Baltes, Ed., *Inverse Scattering Problems in Optics*. New York: Springer-Verlag, 1980.
[2] R. M. Lewis, "Physical optics inverse diffraction," *IEEE Trans. Antennas Propagat.*, vol. AP-24, pp. 308–314, May 1969.
[3] N. N. Bojarski, "A survey of physical optics inverse scattering identity," *IEEE Trans. Antennas Propagat.*, vol. AP-30, pp. 980–989, Sept. 1982.
[4] N. H. Farhat, C. L. Werner, and T. H. Chu, "Prospects for 3-D projective and tomographic imaging radar network," *Radio Sci.*, vol. 19, no. 15, pp. 1347–1355, Sept./Oct. 1984.
[5] N. H. Farhat, "Microwave diversity imaging and automated target identification based on models of neural networks," *Proc. IEEE*, vol. 77, pp. 670–680, May 1989.
[6] R. F. Harrington, *Time-Harmonic Electromagnetic Fields*. New York: McGraw-Hill, 1961.
[7] E. Wolf, "Three-dimensional structure determination of semi-transparent objects from holographic data," *Optics Commun.*, vol. 1, no. 4, pp. 153–156, Sept./Oct. 1969.
[8] R. M. Mersereau and A. V. Oppenheim, "Digital reconstruction of multi-dimensional signals from their projections," *Proc. IEEE*, vol. 62, no. 10, pp. 1319–1338, 1974.
[9] G. T. Ruck, D. E. Barrick, W. D. Stauart, and C. K. Krichbaum, *Radar Cross Section Handbook*. New York: Plenum Press, 1970.

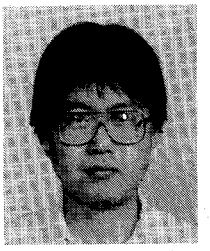

Tah-Hsiung Chu (M'87) was born in Taiwan on July 30, 1953. He received the B.S. degree from the National Taiwan University, Taipei, Taiwan in 1976, and the M.S. and Ph.D. degrees from the University of Pennsylvania in 1980 and 1983 respectively, all in electrical engineering.

From 1983 to 1986 he was a member of technical staff at the Microwave Technology Center of the RCA David Sarnoff Research Center, Princeton, NJ. Since 1986 he has been on the faculty of the Department of Electrical Engineering at the National Taiwan University, where he is now a Professor of Electrical Engineering. His research interests include microwave imaging systems, electromagnetic theory, microwave circuit and subsystem design, microwave measurement techniques, and digital and optical signal processing.

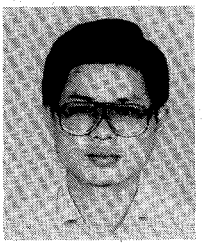

Ding-Bing Lin was born in Taiwan on May 1, 1962. He received the M.S. degree from the National Taiwan University, Taipei, Taiwan, in 1989, and is now working toward the Ph.D. degree. His research deals with microwave imaging systems.